

Automatic Registration of Multisensor Images Using an Integrated Spatial and Mutual Information (SMI) Metric

Jiayong Liang, Xiaoping Liu, Kangning Huang, Xia Li, Dagang Wang, and Xianwei Wang

Abstract—A new image-registration method is presented by integrating the area-based and feature-based methods. The integrated method is characterized by a novel similarity metric based on spatial and mutual information (SMI), the ant colony optimization for continuous domain (ACO_R), and a two-phase searching strategy. The SMI-based metric takes into account both spatial relations of detected features [spatial information (SI)] and the mutual information (MI) between the reference and sensed images. The spatial relation is to derive a fast transformation of the near global optimum without specifying the initial searching range. The MI is to obtain an optimal transformation with high accuracy. ACO_R is adopted to optimize SMI for the first time in this paper, as the function of SMI is generally non-convex and irregular. In addition, a two-phase searching strategy is designed to improve the performance of ACO_R . Phase-1 only considers the SI and finds some low-accurate solutions. Phase-2 considers both SI and MI so it is to search for a more accurate solution. These two phases are switched according to the diversity of the solutions. The proposed integrated method has been tested using the remote-sensing images acquired from different sensors, including TM, SPOT, and SAR. The experimental results indicate that the SMI-based metric is more robust than the conventional metrics which consider SI or MI alone. This method is able to achieve a highly accurate automatic registration of multisensor images.

Index Terms—Ant colony optimization (ACO), image registration, mutual information (MI), remote sensing.

I. INTRODUCTION

IMAGE registration can be described as a process of geometrically aligning two images, the reference image and the sensed image. The registration of remote-sensing images, particularly the multisensor images, is a key component in various applications, such as image mosaicking, image fusion, environmental monitoring, and change detection [1]–[4]. Most of the applications above require high efficiency and accuracy. For instance, a registration accuracy of less than one-fifth of a pixel is required for acquiring a change detection error of

Manuscript received July 9, 2011; revised March 12, 2012, October 17, 2012, and January 17, 2013; accepted January 19, 2013. This work was supported by the China 973 Fundamental Research and Development Project under Grant 2011CB707103 and the National Natural Science Foundation of China (Grant Nos. 40901187).

The authors are with the School of Geography and Planning, and Guangdong Key Laboratory for Urbanization and Geo-simulation, Sun Yat-sen University, Guangzhou 510275, China (e-mail: jiayong1112@163.com; liuxp3@mail.sysu.edu.cn; fytaso@163.com; lixia@mail.sysu.edu.cn; wangdag@mail.sysu.edu.cn; wangxw8@mail.sysu.edu.cn).

Color versions of one or more of the figures in this paper are available online at <http://ieeexplore.ieee.org>.

Digital Object Identifier 10.1109/TGRS.2013.2242895

less than 10% [5]. However, it is challenging for most of the existing methods to satisfy this registration accuracy. On one hand, the traditional image-registration techniques that require manually selected control points (CPs) is very labor intensive and time consuming [6], [7]. On the other hand, the traditional automatic registration algorithms are relatively inefficient, inaccurate, and unstable in the multisensor image registration [8], [9]. It is therefore useful to develop the method to improve efficiency, accuracy and robustness of automatic registration for multisensor images.

There are two major types of automatic registration methods for remote-sensing images: 1) feature-based registration, and 2) area-based registration [1]. The former estimates transformation by matching features extracted from the images, while the latter implements the estimation by using the original intensity information directly.

The feature-based methods are usually utilized when adequate detectable features, appropriate feature extraction, and the matching methods are available. These methods estimate the transformation by matching different kinds of features, including point [8], line [10], and region [11], which are extracted by various feature detection methods, such as Harris corner detector [12], Canny detector [13], image segmentation methods, and phase congruency model [14]. The extracted features are then matched using spatial relations [15], invariant descriptors [16], or relaxation methods [17]. After calculating the value of these feature descriptors for the reference and sensed image, the difference of the value is considered as the distance of the two sets of features. A minimum distance rule with threshold is generally applied [1], [10], [11], [16]. Even without the initial searching range, it is fairly easy for the feature-based methods to find the near-optimal transformation when sufficient distinctive objects are detected [1]. Feature-based methods are capable of registering the images with complex distortions as well as those with distinctive features, such as map and photograph. However, in multisensor remote-sensing image registration, it is difficult for feature detectors to take all the differences of imaging conditions and spectral sensitivity into account [1], which often results in feature mismatching and low registration accuracy.

Usually, the area-based methods are applied when prominent details in the reference and sensed image are not sufficient. With these methods, the entire or subsets of the images are used to estimate the intensity correspondence between them. The correspondence is measured by different kinds of similarity

metrics, such as cross correlation [18], phase correlation [19], and mutual information (MI)[20]. However, the area-based methods often give rise to a heavy computational load, because the statistical dependence between the intensities of the images in these methods is computationally expensive [1], [21]. Moreover, remote-sensing images, which are usually influenced by noise and distortions, are much larger and more complex than general images [8], [22], [23]. Though its use is limited by the extremely heavy computational load and complicated measurement model, the competitive superiority of area-based method is still obvious when it comes to multisensor images. Recent studies [21], [24] have proved that MI-based method can robustly register multisensor images with sub-pixel accuracy. Despite its outstanding performance, the MI-based method provides a local maximum rather than a global maximum of the entire search space for the correct transformation [21], [22]. As a result, a particular region of the search space should be predefined when the MI-based registration is implemented, which inevitably reduces its robustness.

In this paper, we present an integrated method (integration of area-based and feature-based methods) to overcome the respective weaknesses of registration accuracy and computational load. The integration is carried out by proposing a novel similarity metric based on the integrated spatial and MI (SMI). This metric consists of two components, the spatial relations of extracted features [spatial information (SI)] and the MI of image intensity. The component of SI is used to derive a fast transformation of the near global optimum without specifying the initial searching range. The features used to calculate the SI are extracted by the technique based on the phase congruency model [14], which is invariant to illumination and contrast conditions. The component of MI is used to obtain the local optimal transformation with sub-pixel accuracy. The joint histogram for the MI calculation is estimated by partial volume interpolation (PVI) [20].

With a wide range of the initial possible transformation parameters, the global maximum of the proposed metric should be reached when the reference and sensed image are registered. Thus, registering the two images is equivalent to seeking the optimal transformation that maximizes the metric. To find the global optimum of the irregular function of SMI, we first utilize $ACO_{\mathbb{R}}$ as a robust global optimizer for image registration.

Inspired by the real ants' foraging behavior, that the ants deposit pheromone trail on the ground as carrying food to communicate with each other indirectly, Dorigo *et al.* [25] proposed an ant colony optimization algorithm (ACO). As a meta-heuristic, the key component of the original ACO is the pheromone model that allows the artificial ants to cooperate with each other. As a direct extension of ACO, $ACO_{\mathbb{R}}$ [26] is applied to continuous optimization problem (CnOP) when a wide initial possible range is available and higher resolution is required. It uses Gaussian kernel functions as the pheromone distribution model to sample the search space probabilistically. While most traditional techniques tend to trap in local maximum for the non-convex and irregular optimization problems, $ACO_{\mathbb{R}}$ is superior in searching the global maximum. Moreover, a two-phase searching strategy is designed to improve the efficiency of $ACO_{\mathbb{R}}$ in estimating the optimal transformation.

Phase-1 only considers the SI and finds some low-accurate solutions. Phase-2 then considers both SI and MI so it is to search for a more accurate solution. The switch between the two phases is determined by the diversity of the solutions (*div*).

This paper is organized as follows. Section II presents the formulation of the proposed registration method in which the newly proposed metric SMI is described and $ACO_{\mathbb{R}}$ is used to optimize the registration parameters in a two-phase searching strategy. In Section III, we evaluate the proposed method by using multisensor remote-sensing images, including TM, SPOT, and SAR. Finally, Section IV presents conclusions and future works.

II. REGISTRATION BASED ON THE INTEGRATED SMI

This automatic registration model is based on the integrated SMI. First, SI is quantified by the spatial relations of the point features extracted by the phase congruency operator. Meanwhile, the MI is calculated by estimating the joint probability between the two images. Second, the new similarity metric SMI will be constructed by integrating SMI. Finally, $ACO_{\mathbb{R}}$ will be utilized to seek the optimal transformation parameters by a two-phase searching strategy. Fig. 1 is the flowchart of this proposed method. The following section presents the details of the proposed similarity metric and the framework of registration utilizing $ACO_{\mathbb{R}}$.

A. Integrated SMI as Objective Function

As mentioned in Section I, image-registration methods can be divided into area-based methods and feature-based methods. To estimate the correspondence between the reference and sensed image, both methods use a number of similarity metrics, such as the area-based methods described in [18]–[20] and the feature-based methods in [27], [28]. The basic principle of these methods is to find the optimal transformation parameters that maximize (or minimize) the similarity metric. This process can be expressed as

$$\alpha^* = \arg \text{opt} (S (A, T_{\alpha}(B))) \quad (1)$$

where A and B are the images to be registered, T_{α} is the transformation model, α is the transformation parameters, and S represents the similarity metric. The choice of similarity metric is the key to an effective registration model.

Among the similarity measurements mentioned above, the measurements based on spatial relations of features are more classical and sophisticated while MI is regarded as a leading technique in multisensor image registration [1]. However, these methods have limitations when they are used alone. As is summarized in Section I, the spatial relation of features (which will be referred to as SI, in the following text) is difficult to obtain sub-pixel accuracy in multisensor registration, and the MI has a limitation in the need of predefined parameter range. In this paper, we try to overcome these drawbacks by integrating the SI and the MI. The integration is carried out by proposing a novel metric—the integrated SMI.

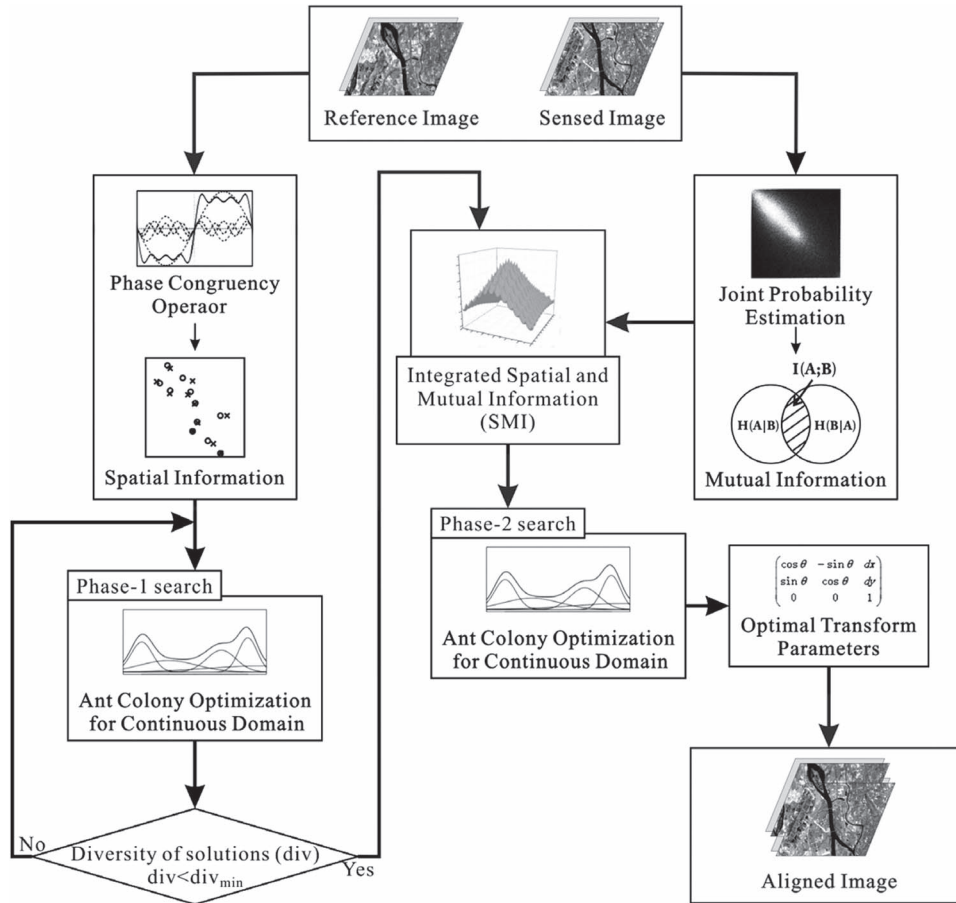


Fig. 1. Flowchart of the proposed method.

The metric SMI considers both the SI and the MI. It is a function of SI and MI, which can be defined as

$$SMI(T_\alpha) = SI_{A,B} \cdot MI_{A,B}. \quad (2)$$

In (2), $SI_{A,B}$ represents the SI of the reference image A and the sensed image B , $MI_{A,B}$ represents the MI. Both of them are functions with respect to the transformation parameters

$$SI_{A,B} = SI(A, T_\alpha(B)) \quad (3)$$

$$MI_{A,B} = MI(A, T_\alpha(B)). \quad (4)$$

Only when both of these two terms are large, then the SMI will reach its maximum. The following sub-sections provide more details on the definition and calculation of SI and MI.

1) *SI*: The SI of SMI is used to efficiently estimate near global-optimal transformation and correct the bias of MI. In the proposed method, the modified Hausdorff distance is used to measure the spatial relations of the extracted features.

The phase congruency model [14] is used to extract similar distributed features from multisensor images. Instead of considering edge as locations with maximal intensity gradient, the phase congruency model regards edge points as where the Fourier components are maximally in phase [29], presented in Fig. 2.

Based on the local-energy model that first introduced by Morrone *et al.* [30], location x 's phase congruency could be

measured by

$$PC(x) = \frac{|E(x)|}{\sum_n A_n(x)} \quad (5)$$

where $|E(x)|$ is the magnitude of the vector sum of all Fourier components, and $A_1(x), A_2(x), \dots, A_n(x)$ are the amplitudes of the local Fourier components [Fig. 2(c)]. When most Fourier components are in phase, $E(x)$ and the sum of $A_1(x), A_2(x), \dots, A_n(x)$ will be aligned approximately, and $PC(x)$ ($0 < PC(x) < 1$) will be large and close to 1.

Later, Kovessi [14] developed a 1-D measurement of phase congruency at location x as

$$PC(x) = \frac{\sum_n W(x) [A_n(x) \Delta\Phi(x) - t]}{\sum_n A_n(x) + \varepsilon} \quad (6)$$

$$\Delta\Phi(x) = \cos(\phi_n(x) - \bar{\phi}(x)) - |\sin(\phi_n(x) - \bar{\phi}(x))|.$$

In the formulas above, $W(x)$ weights for frequency spread, $A_n(x)$ and $\phi_n(x)$ are the amplitude and phase at location (x) at wavelet scale n , $\bar{\phi}(x)$ is the weighted mean phase, t is the estimated noise influence, and ε is a small constant that prevents the division being zero. This measurement has the capabilities of producing a highly localized response and incorporating noise compensation [29], to address the noise sensitivity problem of the former local-energy model. These characteristics make it invariant to image illumination, which also make it suitable for feature extraction in multisensor image registration. To apply this 1-D measurement on image, moments of phase congruency

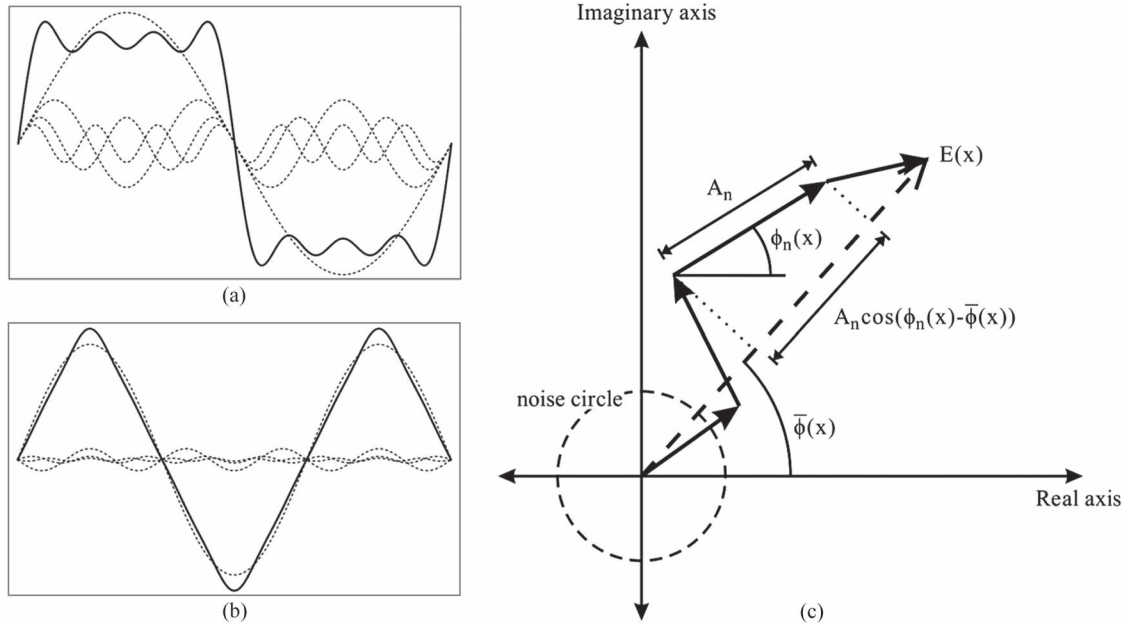


Fig. 2. Square (a) and triangular (b) waveforms in solid lines constructed by four Fourier series in broken lines. The Fourier components are all in phase at the center of the step in (a), and at the peaks and trough in (b). Polar diagram (c) presents the Fourier component, complex vector determined by amplitude $A_n(x)$ and phase $\phi_n(x)$. For location x , its Fourier components are plotted head to tail, and the vector sum of all components is $E(x)$.

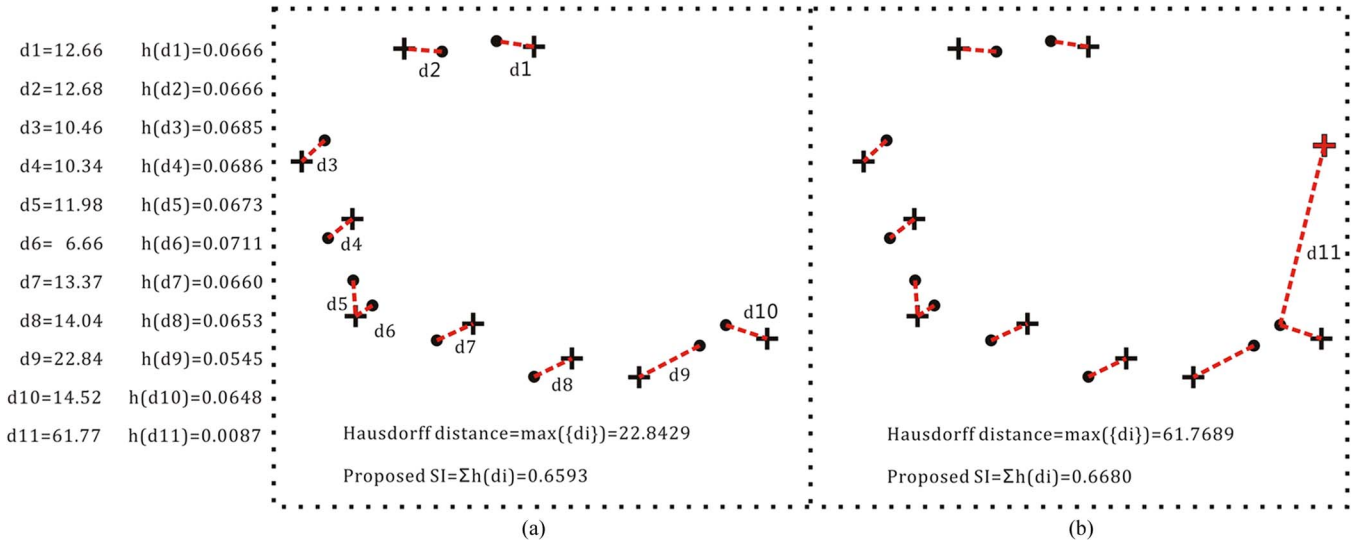


Fig. 3. Hausdorff distance (H) and proposed spatial information (SI) of two similar data sets. With an additional outlier [(a red cross in (b)), H changed from about 22.84 in (a) to 61.77 in (b) and SI slightly increased from about 0.66 in (a) to 0.67 in (b).

are calculated by $PC(x)$ independently in several orientations, through the data obtained by Gabor wavelets. The maximum moment would give the representation of edge features. In this paper, the classical moment analysis techniques are used to find the maximum moment.

After the edge significance is calculated by the phase congruency model, points along the extracted edges are utilized to quantify the similarity of the reference and sensed image by calculating the modified Hausdorff distance between these two point sets (i.e., CP_A and CP_B). The original Hausdorff distance [31] quantifies the point sets' resemblance by measuring the distance of the point in CP_A that is farthest from any nearest point in CP_B . This distance has been applied in image registration [32]–[35] and turned out to be effective. The smaller the distance, the more resemble the two point sets are. Two simple

examples of Hausdorff distance are shown in Fig. 3. Note that in Fig. 3(a), a small distance indicates that the two point sets are similar; whereas in Fig. 3(b), with only one extra outlier, a large Hausdorff distance exaggerates the mismatch. In order to minimize the influence of outliers, we used the sum of the distances as the measurement of resemblance and transform the sum by Gaussian function. This measurement is defined as SI

$$SI_{A,B} = \sum_{cp_A \in CP_A} h \left(\min_{cp_B \in CP_B} \|cp_A - cp_B\| \right) \quad (7)$$

where

$$h(x) = \frac{1}{\sqrt{2\pi}\sigma} \exp \left(-\frac{x^2}{2\sigma^2} \right). \quad (8)$$

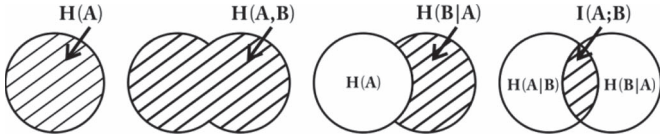


Fig. 4. Venn diagram of the relationship between marginal entropy $H(A)$, joint entropy $H(A, B)$, conditional entropy $H(B|A)$, and mutual information $I(A; B)$.

In the equations above, CP_A and CP_B are the sets of extracted points from the reference and sensed images, respectively. $\|\bullet\|$ denotes the distance between two CPs cp_A, cp_B in 2-D Euclidean space and only the minimal distance of every two points is concerned, leaving no specified requirement for the relationship of CPs' number. $h(x)$ is a standard Gaussian density function with variance σ^2 , which is chosen according to the expectation of distance of corresponding CPs. In Fig. 3, $\sigma = 30$, a pair of points are regarded as CPs with probability of about 0.68 when their distance is within 30 pixels.

This spatial consistency measure is similar but not identical to that used in [28]. A small value of Hausdorff distance between corresponding ground CP sets, excluding the outliers, suggests that the two images are geometrically aligned. The Gaussian functions $h(x)$ used $SI_{A,B}$ regards the outliers as points with extreme distance to others and then rescales it to a smaller value. In this case, most of the Gaussian functions are near their maximums, and $SI_{A,B}$ is maximized. The $SI_{A,B}$ does not only measure the spatial consistency of the extracted features from the two images but also minimizes the influence of outliers. SI is less sensitive to outliers because: 1) the Gaussian function can suppress those outliers' point pairs that have large distances, and 2) the summation is large only when most corresponding point pairs are close to each other. The corresponding values of Hausdorff distance and SI of the examples used in Fig. 3 have been calculated and listed. As can be seen from (7), $SI_{A,B}$ only considers the distance between nearest points. Therefore, the computational complexity of $SI_{A,B}$ is $O(n_{CPs})$, where n_{CPs} is the number of extracted points.

2) *MI*: Proposed by Hartley [36], information entropy is a measure of information contained in a message. Later, Shannon [37] modified Hartley's definition by weighting the outcomes according to the associated occurring probability. To measure the information redundancy of two random variables, A and B , the joint entropy will be used

$$H(A, B) = - \sum_{i,j} p(i, j) \log p(i, j) \quad (9)$$

where $p(i, j)$ is the probability of the occurring of the i th value of random variable A and the j th value of B .

The MI (*MI*) is defined as the information that two random variables A and B contain about each other. The form of MI is defined as

$$MI(A; B) = H(A) + H(B) - H(A, B). \quad (10)$$

The relations between joint entropy $H(A, B)$, marginal entropy $H(A)$ and $H(B)$, conditional entropy $H(B|A)$ and MI $I(A; B)$ are demonstrated in Fig. 4.

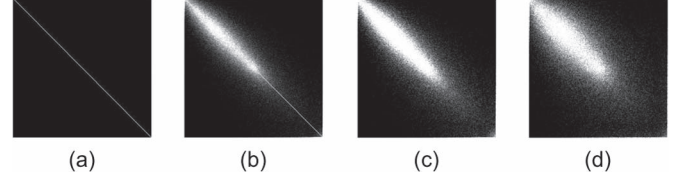


Fig. 5. Gray value of joint histogram of a remote-sensed image with itself. (a) shows the situation that no transformation is performed. (b), (c), and (d) show the corresponding histogram when one image is translated with 0.5, 1, and 2 pixels, respectively.

As a measurement of information that two signals contain about each other, MI is also capable of measuring the information between two images. In the following, the random variable A, B will stand for the referenced image and the sensed image, respectively.

When MI was first introduced to image registration, it was assumed that the two images' corresponding regions are composed of similar intensity values. Then, this similarity is postulated by the average variance of the intensity value ratio of corresponding points [38]. Later, the joint histogram was proposed, which is a 2-D matrix indicating the amount of intensity pairs in the reference and sensed image [39]

$$h = \begin{bmatrix} h(0, 0) & h(0, 1) & \cdots & h(0, N-1) \\ h(1, 0) & h(1, 1) & \cdots & h(1, N-1) \\ \vdots & \vdots & \ddots & \vdots \\ h(M-1, 0) & h(M-1, 1) & \cdots & h(M-1, N-1) \end{bmatrix}. \quad (11)$$

In the joint histogram, $h(a, b)$ ($0 \leq a \leq M-1, 0 \leq b \leq N-1$, where M, N are the range of intensity value of the two images) is the number of pixel pairs with intensity value a in A and intensity value b in B . The major characteristic of joint histogram is that its dispersion increases with the mis-registration of the two images. This characteristic is shown in Fig. 5. In our study, the joint histogram is estimated by PVI proposed by Maes *et al.* [20].

The joint probability distribution is then estimated by (12)

$$p(a, b) = \frac{h(a, b)}{n} \quad (12)$$

where n is the number of pixels in the overlapped area of the two images.

In addition to the original definition as (10), normalized MI (NMI) [40] has been proposed for image registration, which are less sensitive to the size of overlap area

$$NMI(A, B) = \frac{H(A) + H(B)}{H(A, B)}. \quad (13)$$

Defined as a measure of information redundancy between two images, the value of MI is maximal when the two images are geometrically aligned. The computational complexity of NMI is $O(n_{overlap})$, where $n_{overlap}$ is the number of pixels in the overlapped area.

B. ACO for Continuous Domain (ACO_R) as an Optimization Technique

The SMI as an objective function contains many local optimums, which are caused by local good match of extracted

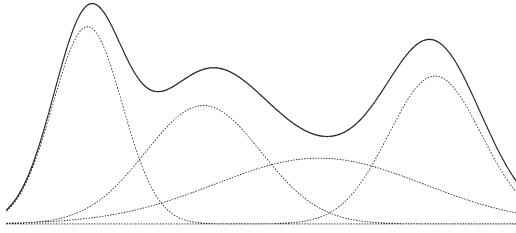


Fig. 6. Gaussian kernel function G^i (the solid line). G^i is the weighted sum of k individual Gaussian PDF, denoting as $g_l^i (l = 1, 2, \dots, k)$ (the broken lines, $k = 4$ as illustrated).

features and the interpolation artifact inherent from MI. Moreover, an automatic registration method should minimize the human supervision of selecting ground CPs or providing a pre-defined initial range of transformation parameters. Therefore, this proposed optimization algorithm should be able to seek the global optimum with sufficiently wide initial range.

In our study, ACO for continuous domain ($ACO_{\mathbb{R}}$) [26] is used as a global optimizer. In implementation, traditional $ACO_{\mathbb{R}}$ faces with difficulties because of involving intensive computation. A two-phase searching strategy is then proposed to improve its efficiency.

1) $ACO_{\mathbb{R}}$ Meta-Heuristic: In general, $ACO_{\mathbb{R}}$ contains three major algorithmic components: 1) solution construction, 2) pheromone update, and 3) daemon action. Components 1) and 2) are to search for a solution based on meta-heuristic; 3) is to determine the iterative stopping condition.

Without loss of generality, a model for CnOP can be defined as: $Q = (X, \Omega, f)$. In this model, an n dimensional optimal solution $s^* \in X$ is generated from the search space $X \subseteq R^n$, with constraints Ω , in order to maximize an objective function $f : X \rightarrow R$. In this case of image registration, X is the transformation parameter (rotation, horizontal, and vertical displacement) and f is the similarity metric, integrated SMI; s^* represents the optimal transformation that maximizes SMI, containing n parameters ($n = 3$ in the experiment). The followings are the details of the three algorithmic components, in the search of s^* .

a) *Ant-Based solution construction*: $ACO_{\mathbb{R}}$ has the solution archive \mathbb{S} to keep track of the solution s , satisfying $s \in X$, where $X = [X_1, X_2, \dots, X_n]^T$ is the search space with constraints Ω . Every new n -dimensional solution is generated by sampling Gaussian kernel probability density function (PDF) $G^i(x) (i = 1, 2, \dots, n)$, respectively. When X_1 represents the horizontal displacement, $G^1(x)$ is the corresponding continuous PDF, where the independent variable is the displacement and the dependent variable its probability density.

With k solutions, define the Gaussian kernel function $G^i (i = 1, 2, \dots, n)$ (Fig. 6) as

$$G^i(x) = \sum_{l=1}^k \omega_l g_l^i(x). \quad (14)$$

The sampling process of X_i requires the *inverse* of $G^i(x)$, which is mathematically difficult to solve. Therefore, selecting one $g_l^i(x)$ from $G^i(x)$'s k components is implemented in practice via an equivalent two-phase sampling.

s_1	s_1^1	s_1^2	\dots	s_1^i	\dots	s_1^n	$f(s_1)$	ω_1
s_2	s_2^1	s_2^2	\dots	s_2^i	\dots	s_2^n	$f(s_2)$	ω_2
	\cdot	\cdot		\cdot		\cdot	\cdot	\cdot
	\cdot		\cdot	\cdot		\cdot	\cdot	\cdot
	\cdot			\cdot		\cdot	\cdot	\cdot
s_l	s_l^1	s_l^2	\dots	s_l^i	\dots	s_l^n	$f(s_l)$	ω_l
	\cdot	\cdot		\cdot		\cdot	\cdot	\cdot
	\cdot		\cdot	\cdot		\cdot	\cdot	\cdot
	\cdot			\cdot		\cdot	\cdot	\cdot
s_k	s_k^1	s_k^2	\dots	s_k^i	\dots	s_k^n	$f(s_k)$	ω_k
	G^1	G^2		G^i		G^n		

Fig. 7. Solution archive \mathbb{S} used in $ACO_{\mathbb{R}}$, with size $k \times n$. Every solution $s_i (i = 1, 2, \dots, k)$ chooses a value for its variable by sampling Gaussian kernel PDF $G^i (i = 1, 2, \dots, n)$. Each of these PDF G^i is determined by the previous solutions and the associated weights $\omega_i (i = 1, 2, \dots, k)$. These weights are depended on the rank of their corresponding objective functions $f(s_i) (i = 1, 2, \dots, k)$.

First, one Gaussian function $g_l^i(x)$ will be chosen probabilistically depending on probability $p_l (l = 1, 2, \dots, k)$ calculated as

$$p_l = \frac{\omega_l}{\sum_{r=1}^k \omega_r}. \quad (15)$$

The p_l is proportion to the weight $\omega_l (l = 1, 2, \dots, k)$. While the weight ω_l is proportional to the quality of the corresponding previous objective function $f(s_l)$, in other words, a Gaussian function associated with better solution will have a greater chance to be chosen. Therefore, as a maximization problem, the weights should satisfy $\omega_1 \geq \omega_2 \geq \dots \geq \omega_l \geq \dots \geq \omega_k$ when $f(s_1) \geq f(s_2) \geq \dots \geq f(s_l) \geq \dots \geq f(s_k)$. In [26], the weights are set by first sorting the solutions $\{s_1, s_2, \dots, s_l, \dots, s_k\}$ according to their respective objective function values $\{f(s_1), f(s_2), \dots, f(s_l), \dots, f(s_k)\}$, and then the weights are calculated according to

$$\omega_l = \frac{1}{qk\sqrt{2\pi}} \exp \left\{ -\frac{(l-1)^2}{2q^2k^2} \right\} \quad (16)$$

where l is the rank of a solution s_l and represents its order in the sorted sequence of all solutions. Above is another Gaussian function with argument l , mean 1.0, and standard deviation qk . In (16), $q (0 < q < 1)$ is a parameter balancing the significance between the iteration-best and the global-best pheromone updating. If $q \rightarrow 0$, the best solution found so far will be used with higher probability in further search. When q is approaching 1, the search will be more diversified and robustly.

Second, the chosen Gaussian function $g_l^i(x)$ is then determined by the mean μ_l^i and variance $(\sigma_l^i)^2$

$$g_l^i(x) = \frac{1}{\sigma_l^i \sqrt{2\pi}} \exp \left\{ -\frac{(x - \mu_l^i)^2}{(\sigma_l^i)^2} \right\}. \quad (17)$$

In (17), μ_l^i and σ_l^i can be calculated from the previous solution archive \mathbb{S} [26] (Fig. 7) as

$$\mu_l^i = s_l^i \quad (18)$$

$$\sigma_l^i = \xi \sum_{e=1}^k \frac{|s_e^i - s_l^i|}{k-1}. \quad (19)$$

It could be noticed that, each Gaussian function $g_l^i(x)$ is centralized at the associated solution s_l , with a standard deviation σ_l^i derived from the average distance from s_l to other solutions $s_e (e = 1, 2, \dots, k)$. The parameter ξ is similar to the evaporation rate of pheromone in original *ACO*, which adjusts the balance between exploitation and exploration. Thus, lower value of ξ will results in higher convergence speed as well as a greater chance to be stuck in local optima, and vice versa.

b) Pheromone update: The pheromone distribution in $ACO_{\mathbb{R}}$, also called the heuristic information, is represented as a series of Gaussian kernel functions, requiring a few parameters stored in the solution archive \mathbb{S} . By the means of changing the solution archive \mathbb{S} , the pheromone distribution is updated.

At the beginning of $ACO_{\mathbb{R}}$, a solution archive \mathbb{S} with k solutions is generated by uniform random sampling. Later at each iteration, a new solution archive S' with m solutions is produced by m ants. In $ACO_{\mathbb{R}}$, it is assumed that each ant carries one solution. These two archives are then united, obtaining $\Delta\mathbb{S} = Rank(\mathbb{S} \cup S')$. In other words, $k + m$ solutions stored in \mathbb{S} and S' will be united and ranked. Before the next iteration, m worst solutions in $\Delta\mathbb{S}$ will be removed to ensure that only the best k solutions could be kept and then effectively guide the coming search process. In this paper, the m worst solutions are regarded as those have smaller value of registration index, SMI, than other k solutions.

c) Daemon actions: After updating the solution archive \mathbb{S} , the best solution found so far is returned. Meanwhile, the termination conditions will be examined. These conditions include the number of iterations, improvement of the objective function, or difference between the best and worst solutions. In this case, when the desired condition, iterations t_{max} , is met, the optimization process will terminate.

2) Two-Phase Searching Strategy: In this paper, $ACO_{\mathbb{R}}$ is used to seek the optimal transformation parameters for translations and rotation so that multisensor remote-sensing images can be registered. The transformation can be expressed as

$$T = \begin{pmatrix} \cos \theta & -\sin \theta & dx \\ \sin \theta & \cos \theta & dy \\ 0 & 0 & 1 \end{pmatrix} \quad (20)$$

where θ is the rotation angle, dx and dy are the horizontal and vertical displacement, respectively. The sensed image B can be registered to the reference image A through the associated transformation T , which is usually denoted as $T(B)$. The search for registration parameters is a CnOP, whose objective function is

$$SMI(T) = SI(A, T(B)) \cdot MI(A, T(B)). \quad (21)$$

As mentioned in Section II, the computational complexity of SI is $O(n_{CPs})$, while that of MI is $O(n_{overlap})$. Suppose the number of iterations is t_{max} , and k solutions are constructed at each iteration, then the total execution time of the proposed method should be $O(t_{max} \cdot k \cdot (n_{CPs} + n_{overlap}))$.

The amount of extracted features should be much less than the amount of the original pixels, thus during the calculation of SMI, we will have $O(n_{CPs}) \ll O(n_{overlap})$. Based on the great difference of efficiency, a two-phase searching strategy is proposed to accelerate the optimization process. In this

strategy, the process is divided into two phases, phase-1 and phase-2. Only SI is considered in SMI at phase-1, while both metrics are considered at phase-2. These two phases share the same solution archive \mathbb{S} , and thus share the same distribution of pheromone. At phase-1, several low-accurate solutions are found, and the pheromone is redistributed around these solutions. Then, at phase-2, this heuristic information is inherent, and $ACO_{\mathbb{R}}$ will continue to search more accurate solutions.

The switch between these two phases is determined by the diversity of the solutions stored at \mathbb{S} . It is found that, when the $ACO_{\mathbb{R}}$ converges, several near-optimal solutions are found and the diversity of \mathbb{S} will decrease [41]. Therefore, the diversity is a suitable measure of convergence and also a reasonable determinant of phase switching. We adopted the measure of diversity used in [41], [42]

$$div(\mathbb{S}) = \frac{1}{N_{diag} \cdot k} \sum_{l=1}^k \sqrt{\sum_{i=1}^D (x_l^i - \bar{x}^i)^2} \quad (22)$$

where N_{diag} is the length of the diagonal of the search space, k is the number of solutions in \mathbb{S} , x_l^i is the component at dimension i of the l th solution at \mathbb{S} , and \bar{x}^i is the average of all the solutions in dimension i . Note that the $\sqrt{\sum_{i=1}^D (x_l^i - \bar{x}^i)^2}$ is simply the Euclidian distance to an average solution \bar{x} , and thus the $(1/k) \sum_{l=1}^k \sqrt{\sum_{i=1}^D (x_l^i - \bar{x}^i)^2}$ gives the average distance to that solution. After dividing the average distance by the diagonal of the search space N_{diag} , $div(\mathbb{S})$ now represents the diversity of solutions in proportion to the parameter ranges. For instance, if $div(\mathbb{S}) = 0.05$ and the searching range of displacement is $[-500, 500]$, then the diversity of solutions is approximately 50. As is suggested in [41], [42], the value of $div(\mathbb{S})$ should be set in the range $[0.0, 0.5]$. The higher value of div , the more diverse is the set of solutions.

Based on this measurement of diversity, the SMI can be modified as a piecewise function

$$SMI(T) = \begin{cases} SI(A, T(B)), & div \geq div_{min} \\ SI(A, T(B)) \cdot MI(A, T(B)), & div < div_{min} \end{cases} \quad (23)$$

When a certain threshold div_{min} is reached, it means the solutions found by the proposed algorithm have converged to a region of the searching space. These solutions are near global optimal. From then on, SMI considers both SMI to seek more accurate solutions. As can be seen from the definition of spatial and NMI as (7) and (13), the value of $MI(A, T(B))$ is in the range $[1.0, 2.0]$, while the value of $SI(A, T(B))$ is positive. Thus, each solution constructed in phase-2 has a higher objective function value than those constructed in phase-1. According to the pheromone update rule, the more accurate solutions will tend to replace the less accurate solutions. This process will continue to converge rather than diverse again. This allows the generation of more accurate transformation at phase-2.

In practice, a rather small value of div_{min} is recommended ($div_{min} = 0.05$ in the experiment). For images with hundreds by hundreds pixels, $div_{min} = 0.05$ indicates that the switch will take place after the diversity of the solutions is less than dozens of pixels. In other word, the algorithm is likely to continue

converging in phase-2, as long as the solutions constructed in phase-1 lie several dozen pixels away from the optimal transformation. Such div_{\min} emphasizes the primary search by SI to ensure high efficiency and satisfies the registration accuracy requirement by MI.

III. IMPLEMENTATION AND RESULTS

This proposed method was examined by registering various types of remote-sensing images from multisensors. They include optical data from Landsat TM, SPOT, and microwave imagery of Radarsat SAR which cover the same study area of Guangzhou, the largest city in south China. Landsat TM and SPOT are passive radiometers which can acquire images only in a cloud-free daylight condition. SAR is a side-looking active synthetic aperture radar instrument, and it is able to obtain data during day or night and even through clouds. Taking advantage of these different types of imagery helps to delineate flooding [43] and mapping forestry [44]. In our experiment, all the images are resampled to the same resolution of the finer one so that registration can be carried out and the proposed metric SMI can be assessed. However, these images could be down-sample to coarse resolution in order to accelerate the registration process. The registration transform is considered as that composed of a 2-D translation (t_x, t_y) and a plane rotation θ .

In Section III-A, two pre-registered images acquired by TM and SPOT are used to validate the effectiveness of the proposed metric. This section also includes the comparison of the performances of the three different similarity metrics (SI, MI, and SMI) mentioned above. Then, in Section III-B, a complete automatic registration of two images taken by TM and SAR, respectively, is carried out to validate the effectiveness of the proposed method using SMI and $ACO_{\mathbb{R}}$.

The proposed algorithm was implemented in Matlab. All the experiments were run on a PC with Intel(R) Core(TM)2 2.33 Gz CPU, and 2 Gb RAM; OS Linux version 2.6.38-8-generic (Ubuntu 11.04).

A. Effectiveness of the Integrated SMI

We validate the performance of SI, MI, and SMI and then demonstrate the effectiveness of SMI as well as the drawbacks of SI and MI. Two images are pre-registered and then simulate a horizontal and a vertical translation. The value of the three different similarity metrics under different translation will be calculated and shown. These simulations will demonstrate the possible searching range and respective accuracy of the registration based on different metrics. The remote-sensing images used to demonstrate the effectiveness of the proposed metric are shown in Fig. 8(a) and (b). Although these two images have similar spectral respond, they are taken at different times, by different platforms, and with different spatial resolutions. Before conducting the experiments, the TM image is manually pre-registered and resampled to the same resolution as the SPOT image. The size of the registered image is 743×950 pixels; the resolution of the TM image is 30 m, and the SPOT is 10 m. To be clarified, in the following experiments, unit of translation is based on the pixels of the finer resolution.

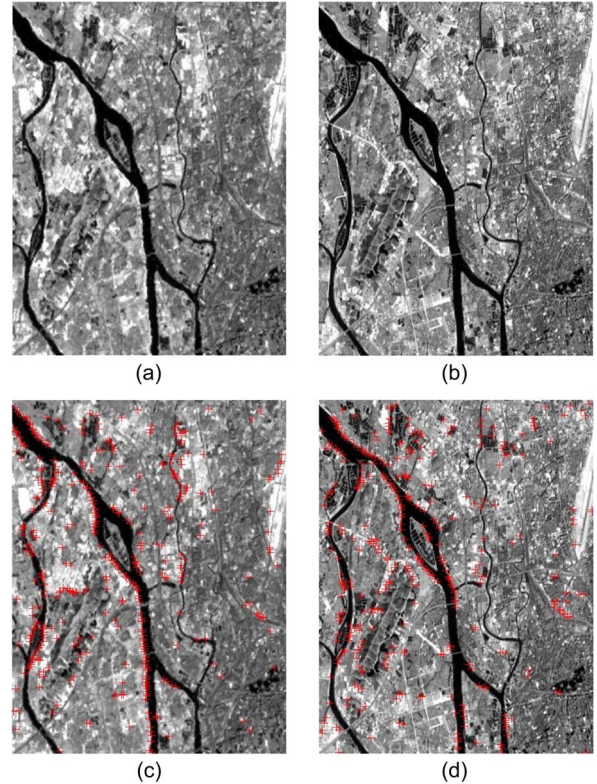


Fig. 8. Images used to demonstrate the effectiveness of the newly proposed metric SMI, which have been manually pre-registered. (a) Sensed image: Landsat TM Band 5, acquired in 2007. (b) Reference image: SPOT Band 4, acquired in 2006. And the CPs extracted by phase congruency model. (c) CPs extracted from sensed image. (d) CPs extracted from reference image.

Although only two images are used, these experiments can be duplicated on any other data set.

A horizontal translation is implemented to demonstrate the estimation bias of SI. To quantify the SI, point features should be extracted by phase congruency model first. The parameters used by phase congruency are listed in the Table I, while the extracted points are shown in Fig. 8(c) and (d). The points as mentioned in Section III-A, the spatial distance of the two sets of point features is used to calculate SI by (7). As is shown in Fig. 9, although the optimal transformation is corresponding to global maximum, it cannot archive sub-pixel accuracy. When checked in detail, the maximal value of SI may not always correspond to the best transform parameters. This issue might be caused by the outliers and feature mismatching. It is common since most of the feature extraction and feature matching methods are not always stable in the registration of multisensor images.

The same translation experiment as that of SI is conducted by using MI. As shown in Fig. 10, the peak of MI is at the point where the reference image and the sensed image are geometrically aligned. Although the correct transformation (without displacement) corresponds to the maximum value of MI, it is at a local maximum within the range between -500 and 500 rather than the global maximum when the size of the image is 743×950 pixels. Affected by the estimation bias of joint probability, the value of MI becomes unreliable as the area of overlapping region decreases. When the NMI is used, our experiments show that the value of the MI will still increase when the overlapped

TABLE I
PARAMETERS USED BY PHASE CONGRUENCY MODEL

Parameters	Images			
	FIG. 8 (c)	FIG. 8 (d)	FIG. 13 (c)	FIG. 13 (d)
Number of wavelet scales	5	5	6	6
Number of filter orientation	3	3	6	6
Wave length of smallest filter	3	3	10	14
Scaling factor between filters	2.5	2.5	1.5	1.5
Stand deviation of Log-Gabor filter	0.55	0.55	3	3
Threshold for non-maximal suppression	0.2	0.16	0.15	0.12

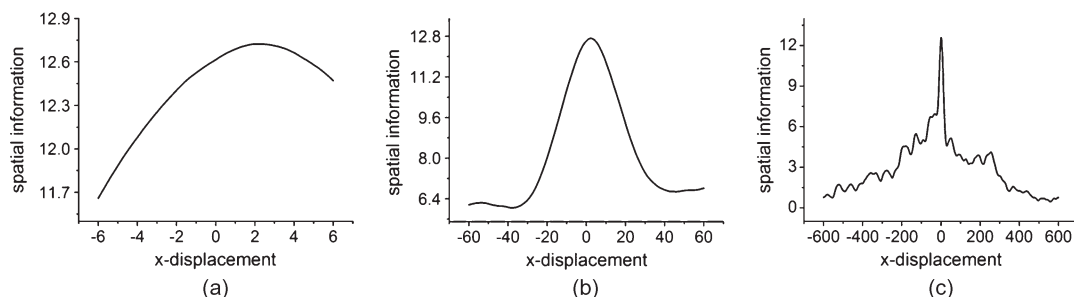


Fig. 9. Spatial information between reference and sensed image in Fig. 8. The sensed image has been translated vertically; this diagram shows the value of SI with respect to x-displacement. (a), (b), and (c) are the SI value when x-displacement is between $[-6, 6]$, $[-60, 60]$, and $[-600, 600]$, respectively.

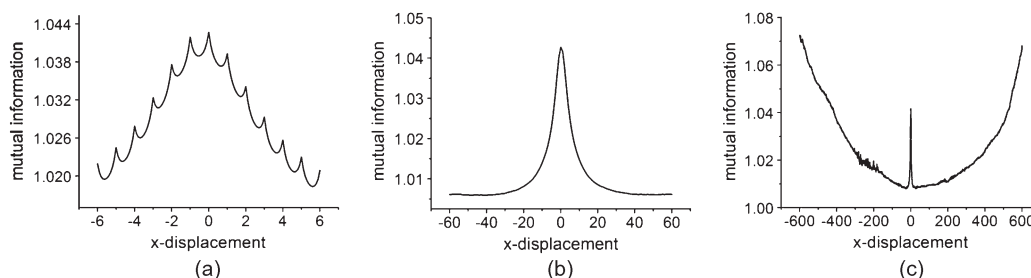


Fig. 10. Mutual information between reference and sensed image shown in Fig. 8. The sensed image has been translated vertically; this diagram shows the value of MI with respect to x-displacement. (a), (b), and (c) are the MI value when x-displacement is between $[-6, 6]$, $[-60, 60]$, and $[-600, 600]$, respectively. Among them, (b) and (c) are sampled by integer translations.

area of two images decreases. When a wide initial range of parameters is given, the algorithms only utilizing MI may fail to find the desired local maximum and produce fault registration results. As can be seen from Fig. 10(c), in this case, only if the initial range is between $[-200, 200]$, successful registration can be guaranteed. Therefore, it is difficult for this model to perform correct registration without any human supervision of giving predefined parameter range.

Another experiment is carried out by utilizing the proposed metric, SMI. The procedures of calculating MI and SI are exactly the same as before, and the SMI is calculated according to (21). Fig. 10(b) and (c) shows that the global maximum of this metric is corresponding to the best transform parameters. Moreover, as shown in Fig. 11(a), SMI also has the capability of archiving sup-pixel accuracy. It must be noticed that, SMI inherit the advantages of both MI and SI. These advantages of SMI show its potential of constructing a highly robust and accurate automatic registration model. Meanwhile, as can be seen from Fig. 11(a), when non-integer translation is performed, plenty of local maxima also state the difficulty of optimization. This difficulty emphasizes the need to introduce $ACO_{\mathbb{R}}$ as a global optimizer.

A further comparison of these three different similarity metrics under 2-D translation is demonstrated in Fig. 12. The features of these metrics are maintained under 2-D translation.

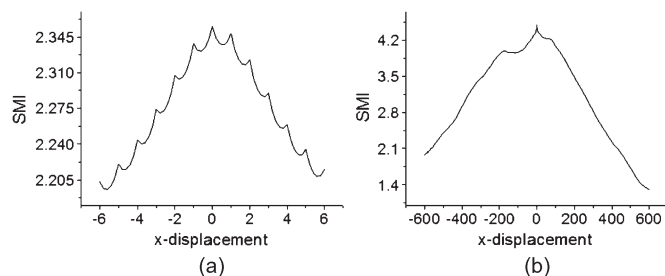


Fig. 11. SMI between reference and sensed image in Fig. 8. The sensed image has been translated vertically; this diagram shows the value of SMI with respect to x-displacement. (a) and (b) are the SMI value when x-displacement is between $[-6, 6]$ and $[-600, 600]$, respectively, where (b) is sampled by integer translations. By seeking the global optimal of this similarity metric, images can be registered with high accuracy and wide initial range of transform parameters.

We can see from Fig. 12(a)–(c) that, SMI shares the global-optimal feature that of SI. Moreover, from Fig. 12(d)–(f), SMI also inherits the high accuracy of MI. SMI is able to overcome their respective drawbacks that SI is difficult to obtain sub-pixel accuracy and MI is in need of predefined parameter range.

In Figs. 10(a), 11(a), 12(d) and (f), the multiple peaks of the MI curves and surfaces are contributed to the interpolation artifacts of MI, which have been discussed in [24], [45]. Avoiding the influence of these artifacts to the greatest extent, the proposed method, with $ACO_{\mathbb{R}}$ and the two phase searching

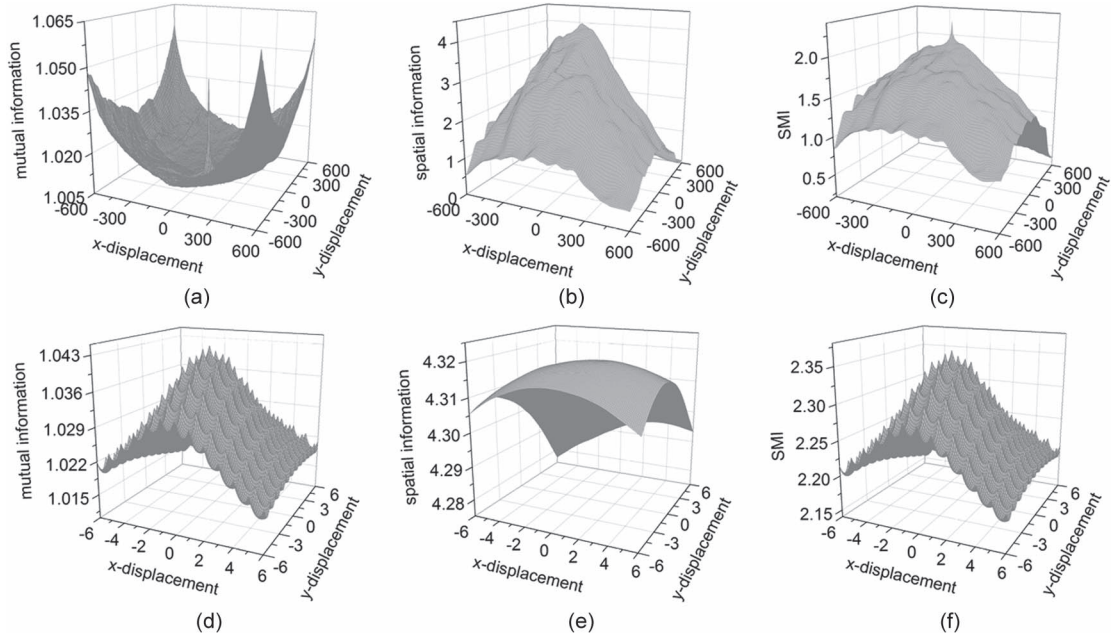


Fig. 12. Surface of three different registration functions under two-dimensional translation. (a)–(c) are the surfaces of MI, SI, and SMI while both x and y displacements are between -600 and 600 pixels. The optimal transformation is the global maximum of both SI and SMI and the local maximum of MI. (d)–(f) are the surfaces of MI, SI, and SMI while both x and y displacements are between -6 and 6 pixels. In this region, the maximum of both MI and SMI is at $(0,0)$, while the maximum of SI is at $(1.3, -2.4)$.

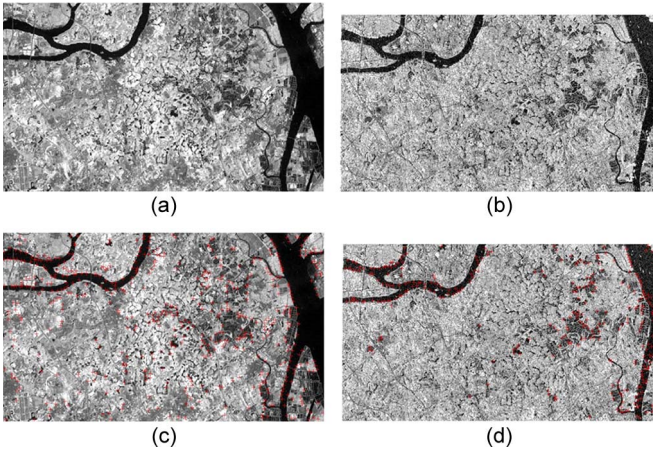


Fig. 13. Images used to validate the effectiveness of the proposed method, and the CPs extracted by phase congruency model. (a) Reference image: Landsat TM Band 4, acquired in 2007. (b) Sensed image: SAR image (HV), acquired in 2008. (c) CPs extracted from reference image. (d) CPs extracted from sensed image.

strategy, seeks the global-optimal transformation. Moreover, the metric SMI is flexible to calculate the MI by higher order generalized partial volume estimation (GPVE) algorithm [46] to further overcome the artifacts problem. The PVI used in this study is regarded as the first-order GPVE algorithm and showed perfect registration consistency and highest efficiency [24]. Although the existence of interpolation artifacts might reduce the registration accuracy, the proposed index, SMI, is flexible to use the second or third GPVE algorithm to quantify MI.

B. Validation of the Proposed Registration Model

To test the reliability and validity of the proposed registration model, an automatic registration without any human supervi-

TABLE II
PARAMETERS USED BY ACO_R

Parameter	Symbol	Value
Number of ants used in an iteration	m	30
Speed of convergence	ξ	1.35
Locality of the search process	q	0.19
Archive size	k	50
Number of iterations	t_{\max}	200
Threshold of diversity	div_{\min}	0.05

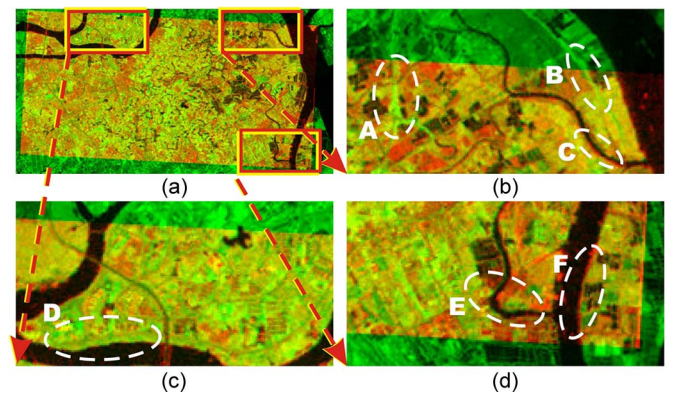


Fig. 14. (a) The registration result. In this RGB color image, the green component is the reference image, and the red component is the registered image. (b), (c), and (d) are the local enlargement areas of the registered image.

sion is performed between two sets of remote-sensing images, a Landsat image (TM4) image (size: 762×397 ; resolution: 30 m) and a SAR image (HV) (size: 696×344 ; resolution: 12.5 m) [Fig. 13(a) and (b)]. These images are acquired by sensors that with different imaging mechanism. As is conducted in Section III-A, these images have been resampled to the same resolution before performing the registration.

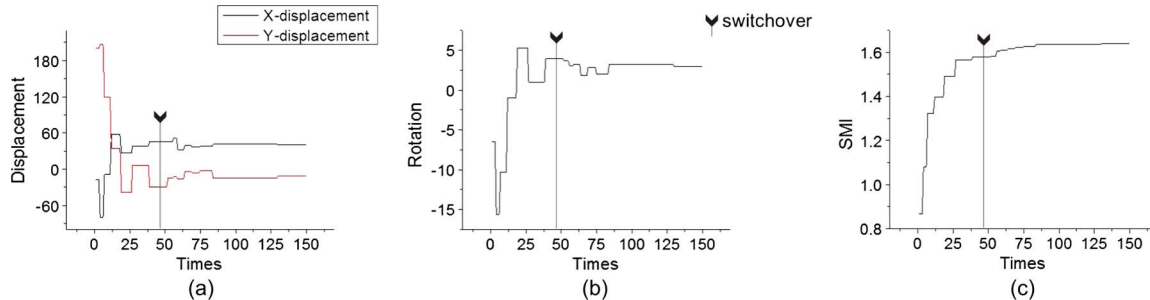


Fig. 15. (a) and (b) are the transform parameters during each iteration, including x-displacement, y-displacement, and rotation. (c) is the value of SMI during each iteration. These values correspond to the best transformation found at each iteration. The switchover presented in the figures indicates that the phase 2 search began at the 47th iteration.

In our experiments, the parameters used for phase congruency model and $ACO_{\mathbb{R}}$ optimization are summarized in Tables I and II. The initial range of rotation is $\theta \in [-180^\circ, 180^\circ]$, and the range of translation is the size of images, i.e., $dx \in [-696, 1458]$, $dy \in [-397, 741]$. Any transformation that is out of this range cannot overlay these two images, which is impossible for image registration. In other words, all possible rotations and translations are included in the search space. Thus, no human supervision is needed for determination of the parameter range. Moreover, the div_{\min} is set to 0.05, which means the switch of phases will take place when the diversity of solutions in x-displacements, y-displacement, and rotation are approximately 100, 50, and 18, respectively. Given the evaluation in Section III-A, SI is able to find solutions several pixels away from the optimal translation. Therefore, the div_{\min} set here is sufficient for the proposed algorithm to converge in phase-2.

Fig. 14(a) shows the result that a Landsat image (TM4) is automatically registered to a SAR image (HV) using this proposed method. This experiment took 6 min, 5.7 s, and 150 iterations. The convergence process is shown in Fig. 15. For better visualization, in Fig. 14, the registration result is shown as an RGB color image, whose green component is the reference image and red component is the sensed image. Although the sensed image is with heavier noise distortion and complete different imaging mechanism compared to the reference image, the proposed method is able to perform an automatic registration without predefined parameter range. Three enlarged parts of the registered image [Fig. 14(a)] are shown in Fig. 14(b)–(d). From these areas, we can find that all the roads [such as A and B in Fig. 14(b)] and most of the river shore [such as D in Fig. 14(c) and E in Fig. 14(d)] are matched. Since these images are acquired at different times, part of the river shore [such as C in Fig. 14(b) and F in Fig. 14(d)] are not completely overlaid. Nevertheless, these local feature differentiations will not influence the global registration, which also indicates the robustness of the proposed method.

IV. CONCLUSION AND FUTURE WORKS

Image registration is a fundamental process of geometrically aligning two images, which are usually acquired from different sensors or at different times. Various applications require high accuracy of multisensor registration results. Traditional techniques have limitations of image registration. These existing techniques can be divided into two categories, the area-based

methods and the feature-based methods. The heavy computational load limits the use of area-based methods, while the accuracy of feature-based methods is usually influenced by different spectral sensitivity. Thus, we tried to integrate them to overcome their drawbacks.

This work represents the first attempt to use the SI of extracted point features in conjunction with MI of intensities to register remote-sensing images. These two kinds of information are integrated by proposing a novel similarity metric—SMI. The global maximum of SMI corresponds to a transformation with sub-pixel accuracy. To optimize the SMI metric, we applied the ant colony algorithm on continuous domain ($ACO_{\mathbb{R}}$) into the transformation parameters estimation for the first time. Moreover, we designed a two-phase searching strategy to improve the optimization efficiency after analyzing the computational complexity of SMI. Combining the SMI metric, $ACO_{\mathbb{R}}$, and the two-phase searching strategy together formulated an automatic registration approach for multisensor remote-sensing images. This approach can effectively reduce human labor and thus improves the efficiency of remote-sensing image processing.

To validate our registration approach, we applied it to the registration of remote-sensing images derived from Landsat TM, SPOT, and SAR. The experimental results indicate that this registration approach can achieve sub-pixel accuracy without predefining the parameter range with a relative satisfactory speed. It took about 6 min to complete the registration process with the size 397×762 of the reference image. This proposed method works well with all possible translations, when the MI-based registration model [47] in which the offsets must be within 24 pixels and [48] that require 10 pixels and 10° offsets. Moreover, unlike the feature-based method—ARRSI system [8]—that require the rotations between $[-30^\circ, 30^\circ]$, our method can handle the optimal transformation with rotations between $[-180^\circ, 180^\circ]$. These features substantially reduce human supervision of selecting ground CPs and greatly improve its robustness in multisensor image registration.

Our automatic registration approach still has some operational limitations. We simplify the image distortion as a 2-D translation and a plane rotation, which may be inconsistent with reality. During the registration process, some parameters are determined by references or repeated experiments. The future study will concentrate on determining the parameters' range of the proposed method automatically, and more attention will be paid on utilizing more advanced SI of extracted features

and new presentation of MI of the two images. The higher order GPVE to MI computation would be carefully considered to balance registration accuracy and efficiency. Moreover, the local distortion of the image should be taken into consideration.

REFERENCES

- [1] B. Zitová and J. Flusser, "Image registration methods: A survey," *Image Vis. Comput.*, vol. 21, no. 11, pp. 977–1000, Oct. 2003.
- [2] X. Liu, X. Li, L. Liu, J. He, and B. Ai, "An innovative method to classify remote-sensing images using ant colony optimization," *IEEE Trans. Geosci. Remote Sens.*, vol. 46, no. 12, pp. 4198–4208, Dec. 2008.
- [3] X. Liu, X. Li, and X. Zhang, "Determining class proportions within a pixel using a new mixed-label analysis method," *IEEE Trans. Geosci. Remote Sens.*, vol. 48, no. 4, pp. 1882–1891, Apr. 2010.
- [4] Z. Li, S. Papson, and R. M. Narayanan, "Data-level fusion of multilook inverse synthetic aperture radar images," *IEEE Trans. Geosci. Remote Sens.*, vol. 46, no. 5, pp. 1394–1406, May 2008.
- [5] X. Dai and S. Khorram, "The effects of image misregistration on the accuracy of remotely sensed change detection," *IEEE Trans. Geosci. Remote Sens.*, vol. 36, no. 5, pp. 1566–1577, Sep. 1998.
- [6] A. D. Ventura, A. Rampini, and R. Schettini, "Image registration by recognition of corresponding structures," *IEEE Trans. Geosci. Remote Sens.*, vol. 28, no. 3, pp. 305–314, May 1990.
- [7] Z. Liu, J. An, and Y. Jing, "A simple and robust feature point matching algorithm based on restricted spatial order constraints for aerial image registration," *IEEE Trans. Geosci. Remote Sens.*, vol. 50, no. 2, pp. 514–527, Feb. 2012.
- [8] A. Wong and D. A. Clausi, "ARRSI: Automatic registration of remote-sensing images," *IEEE Trans. Geosci. Remote Sens.*, vol. 45, no. 5, pp. 1483–1493, May 2007.
- [9] C. A. Shah, Y. Sheng, and L. C. Smith, "Automated image registration based on pseudoinvariant metrics of dynamic land-surface features," *IEEE Trans. Geosci. Remote Sens.*, vol. 46, no. 11, pp. 3908–3916, Nov. 2008.
- [10] H. Li, B. S. Manjunath, and S. K. Mitra, "A contour-based approach to multisensor image registration," *IEEE Trans. Image Process.*, vol. 4, no. 3, pp. 320–334, Mar. 1995.
- [11] A. Goshtasby, G. C. Stockman, and C. V. Page, "A region-based approach to digital image registration with subpixel accuracy," *IEEE Trans. Geosci. Remote Sens.*, vol. GRS-24, no. 3, pp. 390–399, May 1986.
- [12] H. Chris and S. Mike, "A combined corner and edge detector," in *Proc. Fourth Alvey Vis. Conf.*, 1988, pp. 147–152.
- [13] C. John, "A computational approach to edge detection," *IEEE Trans. Pattern Anal. Mach. Intell.*, vol. PAMI-8, no. 6, pp. 679–698, Nov. 1986.
- [14] P. Kovsesi, "Phase congruency: A low-level image invariant," *Psychol. Res.*, vol. 64, no. 2, pp. 136–148, Dec. 2000.
- [15] G. Borgefors, "Hierarchical chamfer matching: A parametric edge matching algorithm," *IEEE Trans. Pattern Anal. Mach. Intell.*, vol. 10, no. 6, pp. 849–865, Nov. 1988.
- [16] J. Flusser and T. Suk, "A moment-based approach to registration of images with affine geometric distortion," *IEEE Trans. Geosci. Remote Sens.*, vol. 32, no. 2, pp. 382–387, Mar. 1994.
- [17] S. Ranade and A. Rosenfeld, "Point pattern matching by relaxation," *Pattern Recognit.*, vol. 12, no. 4, pp. 269–275, 1980.
- [18] N. Hanaizumi and S. Fujimur, "An automated method for registration of satellite remote sensing images," in *Proc. IGARSS—Better Understanding Earth Environment*, 1993, vol. 3, pp. 1348–1350.
- [19] Q. Chen, M. Defrise, and F. Deconinck, "Symmetric phase-only matched filtering of Fourier-Mellin transforms for image registration and recognition," *IEEE Trans. Pattern Anal. Mach. Intell.*, vol. 16, no. 12, pp. 1156–1168, Dec. 1994.
- [20] F. Maes, A. Collignon, D. Vandermeulen, G. Marchal, and P. Suetens, "Multimodality image registration by maximization of mutual information," *IEEE Trans. Med. Imag.*, vol. 16, no. 2, pp. 187–198, Apr. 1997.
- [21] K. Johnson, A. Cole-Rhodes, I. Zavorin, and J. Le Moigne, "Mutual information as a similarity measure for remote sensing image registration," in *Proc. SPIE*, Orlando, FL, USA, 2001, pp. 51–61.
- [22] A. A. Cole-Rhodes, K. L. Johnson, J. LeMoigne, and I. Zavorin, "Multiresolution registration of remote sensing imagery by optimization of mutual information using a stochastic gradient," *IEEE Trans. Image Process.*, vol. 12, no. 12, pp. 1495–1511, Dec. 2003.
- [23] H. Xie, L. E. Pierce, and F. T. Ulaby, "Mutual information based registration of SAR images," in *Proc. IEEE IGARSS*, 2003, vol. 6, pp. 4028–4031.
- [24] H.-M. Chen, P. K. Varshney, and M. K. Arora, "Performance of mutual information similarity measure for registration of multitemporal remote sensing images," *IEEE Trans. Geosci. Remote Sens.*, vol. 41, no. 11, pp. 2445–2454, Nov. 2003.
- [25] M. Dorigo and V. Maniezzo, "Ant system: Optimization by a colony of cooperating agents," *IEEE Trans. Syst., Man, Cybern. B, Cybern.*, vol. 26, no. 1, pp. 29–41, Feb. 1996.
- [26] K. Socha and M. Dorigo, "Ant colony optimization for continuous domains," *Eur. J. Oper. Res.*, vol. 185, no. 3, pp. 1155–1173, Mar. 2008.
- [27] Y. Keller and A. Averbuch, "Implicit similarity: A new approach to multi-sensor image registration," in *Proc. IEEE Comput. Soc. Conf. CVPR*, 2003, pp. II-543–II-548.
- [28] G. J. Wen, J.-J. Lv, and W.-X. Yu, "A high-performance feature-matching method for image registration by combining spatial and similarity information," *IEEE Trans. Geosci. Remote Sens.*, vol. 46, no. 4, pp. 1266–1277, Apr. 2008.
- [29] P. Kovsesi, "Phase congruency detects corners and edges," in *Proc. Aust. Pattern Recognit. Soc. Conf. DICTA*, 2003, pp. 309–318.
- [30] M. C. Morrone and R. A. Owens, "Feature detection from local energy," *Pattern Recognit. Lett.*, vol. 6, no. 5, pp. 303–313, Dec. 1987.
- [31] D. P. Huttenlocher, G. A. Klanderman, and W. J. Rucklidge, "Comparing images using the Hausdorff distance," *IEEE Trans. Pattern Anal. Mach. Intell.*, vol. 15, no. 9, pp. 850–863, Sep. 1993.
- [32] H. S. Alhichri and M. Kamel, "Multi-resolution image registration using multi-class Hausdorff fraction," *Pattern Recognit. Lett.*, vol. 23, no. 1–3, pp. 279–286, Jan. 2002.
- [33] T. Hrkač, Z. Kalafatic, and J. Krapac, "Infrared-visual image registration based on corners and hausdorff distance," in *Proc. Image Anal.*, 2007, pp. 383–392.
- [34] X. Peng, W. Chen, and Q. Ma, "Feature-based nonrigid image registration using a Hausdorff distance matching measure," *Opt. Eng.*, vol. 46, no. 5, pp. 057201-1–057201-16, 2007.
- [35] J. W. Zhang, G.-Q. Han, and Y. Wo, "Image registration based on generalized and mean Hausdorff distances," in *Proc. Int. Conf. Mach. Learn. Cybern.*, 2005, pp. 5117–5121.
- [36] R. V. L. Hartley, "Transmission of information," *Bell Syst. Techn. J.*, p. 535, Jul. 1928.
- [37] C. E. Shannon, "A mathematical theory of communication," *Bell Syst. Techn. J.*, vol. 27, pp. 379–423, Oct. 1948.
- [38] J. B. A. Maintz, M. A. Viergever, and J. P. W. Pluim, "Mutual information based registration of medical images: A survey," *IEEE Trans. Med. Imag.*, vol. 22, no. 8, pp. 986–1004, Aug. 2003.
- [39] A. Collignon, F. Maes, D. Delaere, P. Vandermeulen, P. Suetens, and G. Marchal, "Automated multi-modality image registration based on information theory," in *Proc. Inf. Process. Med. Imag.*, 1995, pp. 263–274.
- [40] C. Studholme, D. L. G. Hill, and D. J. Hawkes, "An overlap invariant entropy measure of 3D medical image alignment," *Pattern Recognit.*, vol. 32, no. 1, pp. 71–86, Jan. 1999.
- [41] G. Leguizamón and C. A. Coello Coello, "A study of the scalability of ACO_R for continuous optimization problems," Departamento de Computación, CINVESTAV-IPN, Mexico, Mexico, Tech. Rep. EVOCINV-01-2010, 2010.
- [42] R. Ursem, "Diversity-guided evolutionary algorithms," in *Parallel Problem Solving from Nature—PPSN VII*, vol. 2439, J. Guervós, P. Adamidis, H.-G. Beyer, J.-L. Fernandez-Villacanas, and H.-P. Schwefel, Eds. Berlin, Germany: Springer-Verlag, 2002, pp. 462–471.
- [43] K. Sivaprasad and R. L. Bolus, "Delineation of 1993 Midwest flooding using ERS-1 SAR, SPOT and Landsat imagery," in *Proc. IGARSS—Surface Atmospheric Remote Sensing: Technologies, Data Analysis Interpretation*, 1994, vol. 3, pp. 1439–1441.
- [44] J. P. Pedersen, T. Guneriusen, and B. Johansen, "Application of ERS-1 SAR data in combination with Landsat and SPOT data for forestry mapping in a Norwegian forest region," in *Proc. IGARSS—Better Understanding Earth Environment*, 1993, vol. 1, pp. 46–48.
- [45] J. P. W. Pluim, J. B. Antoine Maintz, and M. A. Viergever, "Interpolation artefacts in mutual information-based image registration," *Comput. Vis. Image Understand.*, vol. 77, no. 2, pp. 211–232, Feb. 2000.
- [46] H. Chen and P. K. Varshney, "Mutual information-based CT-MR brain image registration using generalized partial volume joint histogram estimation," *IEEE Trans. Med. Imag.*, vol. 22, no. 9, pp. 1111–1119, Sep. 2003.
- [47] J. P. Kern and M. S. Pattichis, "Robust multispectral image registration using mutual-information models," *IEEE Trans. Geosci. Remote Sens.*, vol. 45, no. 5, pp. 1494–1505, May 2007.
- [48] H. Ghorbani and A. A. Beheshti, "Multiresolution registration of multi-temporal remote sensing images by optimization of mutual information using a simulated annealing based Marquardt-Levenberg technique," in *Proc. ICIAAS*, 2007, pp. 685–690.



Jiayong Liang received the B.S. degree in geographical information science from Sun Yat-sen University, China, in 2011. She is working toward the Master's degree in Sun Yat-sen University, Guangzhou.

Her current research interests include remote-sensing technology and its interdisciplinary applications of earth resources and environment.



Xiaoping Liu received the B.S. degree in geography from Sun Yat-sen University, Guangzhou, China, in 2002, and the Ph.D. degree in remote sensing and geographical information sciences from Sun Yat-sen University, Guangzhou, in 2008.

He is a Professor with the School of Geography and Planning, Sun Yat-sen University, Guangzhou. His current research interests include image processing, artificial intelligence, and geographical simulation.



Kangning Huang received the B.S. degree in geographical information science from Sun Yat-sen University, Guangzhou, China, in 2011. He is working toward the Master's degree in Sun Yat-sen University, Guangzhou.

His current research interests include image processing, feature extraction, data assimilation, artificial intelligence, and multi-objective spatial optimization.



Xia Li received the B.S. and M.S. degrees from Peking University, Beijing, China, and the Ph.D. degree in GIS from University of Hong Kong, Hong Kong.

He is a Professor and the Director of the Center for Remote Sensing and Geographical Information Sciences, School of Geography and Planning, Sun Yat-sen University, Guangzhou, China. He is also a Guest Professor in the Department of Geography at the University of Cincinnati, Cincinnati, OH. He got the ChangJiang scholarship and the award of the

Distinguished Youth Fund of the National Science Foundation of China in 2005. His major research interests include remote sensing, geographical information systems for environmental modeling and land use planning, simulation of urban growth and land use changes with cellular automata and geographical information sciences (GIS), radar remote sensing for urban applications, and land use changes and agricultural land loss in the Pearl River Delta. Dr. Li is on the editorial board of the international journal, *GeoJournal*. He is an Associate Editor of the Chinese journal, *Tropical Geography*. He has about 170 articles, of which many appeared in international journals. His papers are widely published in top international GIS and remote-sensing journals, such as *Remote Sensing of Environment*, *International Journal of Remote Sensing*, *Photogrammetric Engineering and Remote Sensing*, *International Journal of Geographical Information Science*, *Environment and Planning A*, and *Environment and Planning B*.



Dagang Wang received the B.S. degree in hydraulic engineering from the Dalian University of Technology, Dalian, China, in 1997, the M.S. degree in hydrology and water resources from the Dalian University of Technology, Dalian, in 2002, and the Ph.D. degree in hydrology and water resources from the University of Connecticut, Storrs, CT, in 2007.

He is an Associate Professor with the School of Geography and Planning, Sun Yat-sen University, Guangzhou, China. His current research interests include effect of urbanization on climate,

land-atmosphere interactions, and land surface modeling.



Xianwei Wang received the B.S. degree from Sichuan Normal University, Sichuan, China, in 1999, the M.S. degree from the South China Sea Institute of Oceanology, Chinese Academy of Sciences, Guangzhou, China, in 2002, and the Ph.D. degree from the University of Texas at San Antonio, TX, USA, in 2008.

He is an Associate Professor at the School of Geography and Planning, Sun Yat-sen University, Guangzhou, China. His current research primarily focuses on surface hydrology, hydrometeorology, and global change using remote sensing and geographic information techniques.